Simulation of profile evolution from ramp-up to ramp-down and optimization of tokamak plasma termination with the RAPTOR code

A A Teplukhina[1], O Sauter[1], F Felici[2], A Merle[1], D Kim[3], the TCV team[a], the ASDEX-Upgrade team[b] and the EUROfusion MST1 Team[c]

[1] École Polytechnique Fédérale de Lausanne (EPFL), Swiss Plasma Center (SPC), CH-1015 Lausanne, Switzerland

[2] Eindhoven University of Technology, POBox 513, 5600MB Eindhoven, The Netherlands

[3] ITER Organization, Route de Vinon-sur-Verdon, CS 90 046, 13067, St. Paul-lez-Durance, France

[a] See the author list of S. Coda et al, Nucl. Fusion 57 (2017) 102011

[b] See the author list of A. Kallenbach et al, Nucl. Fusion 57 (2017) 102015

[c] See the author list of H. Meyer et al, 2017 Nucl. Fusion 57 (2017) 102014

E-mail: anna.teplukhina@epfl.ch

Abstract. The present work demonstrates the capabilities of the transport code RAPTOR as a fast and reliable simulator of plasma profiles for the entire plasma discharges, i.e. from ramp-up to ramp-down. This code focuses, at this stage, on the simulation of electron temperature and poloidal flux profiles using prescribed equilibrium and some kinetic profiles. In this work we extend the RAPTOR transport model to include a time-varying plasma equilibrium geometry and verify the changes via comparison with the ATSRA code simulations. In addition a new ad-hoc transport model based on constant gradients and suitable for simulations of L-H and H-L-modes transitions has been implemented into the RAPTOR code and validated with rapid simulations of the time evolution of the safety factor and the electron temperature over the entire AUG and TCV discharges.

An optimization procedure for the plasma termination phase has been also developed during this work. We define the goal of the optimization as ramping down the plasma current as fast as possible while avoiding any disruptions caused by reaching physical or technical limits. Our numerical study of this problem shows that a fast decrease of the plasma elongation during the current ramp-down can help in reducing the plasma internal inductance. An early transition from H- to L-mode allows to reduce the drop in poloidal beta which is also important for plasma MHD stability and control. This work shows how these complex nonlinear interactions can be optimized automatically using relevant cost functions and constraints. Preliminary experimental results for TCV are demonstrated.

Keywords: transport modeling, electron heat diffusivity, plasma termination, ramp-down optimization

1. Introduction

Scenario development for most existing tokamaks is focusing on the flat top, high performance phase of a plasma discharge, where the main plasma characteristics like MHD stability and particle confinement are investigated. For future tokamaks, fusion reactions will take place during this phase. However the initial and termination phases of a discharge, i.e. phases of plasma current ramp-up and ramp-down and entering or leaving the burning phase, are equally important for tokamak operation. Stabilization of plasma shape and position and a proper kinetic pressure/power balance have to be reached during the initial stage of a plasma discharge. The main goal of the last stage of a plasma discharge is a safe plasma shut-down, which includes a termination from the burning phase in case of presence of fusion during the main phase. For a successful tokamak operation plasma must be well controlled during all these phases. Development of feedback controllers and their integration to tokamaks' magnetic and kinetic control systems is an essential part of ongoing experimental plasma research [1, 2, 3]. Numerical physics-based models are required for these purposes. This paper contributes to the development of reliable physical models for a plasma termination phase. Non-disruptive termination scenarios are important for successful operation of future tokamaks and especially for ITER. Indeed significant heat fluxes to the wall are expected during disruptions because of the large amount of energy stored in burning plasmas. Therefore the main goal of the development of termination scenarios is to find a way to ramp down a plasma current, I_p, as fast as possible while avoiding any disruptions, i.e. an optimal termination trajectory has to be determined. The forces are proportional to I_p^2 in case of disruptions which is why it has to be reduced quickly [4].

Presently development of termination scenarios for different tokamaks is carried out both by experimental and numerical studies. Full discharge simulations with the DINA [5]/CRONOS [6] codes and with the CORSICA [7]/DINA codes have been performed for ITER [8, 9]. Termination phase studies with the JETTO code [10] have been obtained for JET [11, 12]. For better understanding of transport in the current ramp phases, numerical studies with the ASTRA code [13] have been performed for the ASDEX Upgrade tokamak (AUG) [14, 15]. In the present work, we show that the updated RAPTOR code (RApid Plasma Transport simulatoR) [16, 17] can be used for fast simulations of entire discharges and for ramp-down optimization studies for the TCV and AUG tokamaks. RAPTOR has been developed focusing on simplicity and speed of simulations for real-time control purposes [18, 19]. The physical model is simplified in comparison to the ASTRA one, nevertheless it provides good results for real-time control and off-line plasma studies. One of the advantages of the RAPTOR code is the speed of the numerical calculations. A simulation, with 1 ms time-steps, of a TCV plasma discharge on a standard PC takes less than 1 min for a shot 1 s long. Thus, due to its short wall-clock simulation time, the RAPTOR code is an efficient tool for automated ramp-down optimization, since many termination trajectories can be tested in a reasonable time.

This paper is divided into two main parts. Section 2 is related to the RAPTOR transport model development and a new electron heat diffusivity model which has been included. Results of profile evolution simulations of entire discharges for the TCV and AUG tokamaks are presented. Section 3 is focusing on the problem of ramp-down optimization and preliminary results for TCV and AUG discharges are presented. We conclude this paper in section 4.

2. Improving physics fidelity of RAPTOR: time-varying geometry, new electron heat diffusivity model

As it was mentioned above, the present work is performed mainly with the RAPTOR code. It is a light and fast transport code with a simplified transport model and without a solver of the Grad-Shafranov equation since it uses prescribed equilibrium data. However we have extended RAPTOR to be able to easily use a series of equilibria computed by the CHEASE [20] Grad-Shafranov solver which reproduces the time evolution of the plasma shape and profiles. In real-time, it can be taken from a real-time equilibrium reconstruction code like LIUQE [21] which uses constraints from a diamagnetic loop (DML) in adition to the standard magnetic measurements. This approach allows to maintain a reduced CPU time while improving accuracy of the simulation. The RAPTOR transport model includes the diffusion equations for electron temperature and poloidal flux. Up to now the plasma equilibrium was assumed to be fixed [16]. During this work, the transport model has been extended to include a time-varying plasma equilibrium geometry, increasing the accuracy of full discharge simulations.

Additionally a new adhoc model for electron thermal transport has been implemented into the RAPTOR code and tested during this work. This model is based on the fact that the normalized inverse scale of the electron temperature profile R/L_{Te} is almost constant in the core region, whereas the edge region can be described with a constant gradient of the electron temperature profile T_e, when using the appropriate radial coordinate ρ_{tor} or ρ_V [22, 23]. Thus for the core region we prescribe a constant logarithmic gradient, whereas the pedestal height is defined by the given H factor. It was first developed in [24] and used for ITER simulations with ASTRA. Internal transport barriers are not taken into account here but can easily be included. The advantage of this model is twofold. On the one hand it is very simple and fast. On the other hand it depends only on a few characteristics which can be easily related to experimental measurements and thus checked, like the H factor relating the experimental or predicted global confinement time to a given scaling law and the expected profile of inverse scale length in the core plasma region. This limits in a large part "unexpected" small or large local gradients and therefore much more robust predictions for $T_e(\rho, t)$ (and in a later stage $n_e(\rho, t)$).

In this paper only the predictive offline applications of the model are presented. As it as mentioned above, for this we need the prescribed model parameters based on the experimental measurements. However, in real-time differences between estimated from

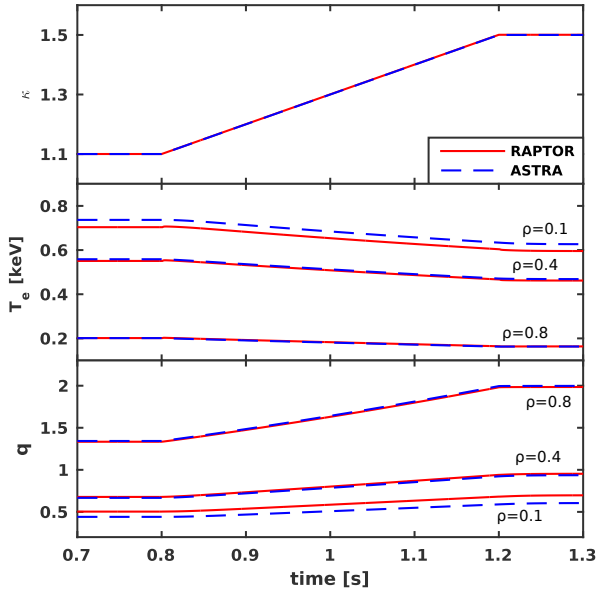

Figure 1. Comparison of RAPTOR and ASTRA simulation results for TCV-like ohmic plasma: time evolution of electron temperature T_e and safety factor q at radial positions $\rho_{tor} = [0.1,\ 0.4,\ 0.8]$ in case of a time-varying plasma boundary elongation κ.

the measurements and prescribed model parameters R/L_{Te} and H_e can give important information on the plasma state. In particular, strongly increased measured R/L_{Te} can reflect presence of ITBs, and decrease in real-time H_e (H factor for electrons only) can be caused by impurity accumulation. Moreover, thanks to the approach's speed, the model parameters can also be updated in real-time. This allows to the electron temperature profile T_e from simulations to evolve with an actual plasma state, thus providing more reliable information to the control systems. See the following discussion in Sec. 2.3.

We describe first the new equations solved by RAPTOR in Sec 2.1, where the results are checked with ASTRA, then the implementation of the new transport model based on [24] in Sec 2.2, the simulation results and their comparison to experimental data are presented in Sec. 2.3, discussion on ramp-down simulations is in Sec. 2.4.

2.1. The transport model with time-varying terms

The RAPTOR transport model is now based on the two transport equations for T_e and ψ, as presented in the ASTRA code [13]. These equations can be rewritten including normalized enclosed toroidal coordinate $\hat{\rho} = \rho/\rho_b$ and normalized enclosed toroidal flux $\hat{\Phi} = \Phi/\Phi_b$ where $\Phi = \pi B_0 \rho^2$, and the index "b" is used for boundary values:

- diffusion equation for the poloidal flux:

$$\sigma_{\parallel}\left(\left.\frac{\partial\psi}{\partial t}\right|_{\hat{\rho}} - \frac{\hat{\rho}\dot{\Phi}_b}{2\Phi_b}\frac{\partial\psi}{\partial\hat{\rho}}\right) = \frac{F^2}{16\pi^2\mu_0\Phi_b^2\hat{\rho}}\frac{\partial}{\partial\hat{\rho}}\left[\frac{g_2 g_3}{\hat{\rho}}\frac{\partial\psi}{\partial\hat{\rho}}\right] - \frac{B_0}{2\Phi_b\hat{\rho}}V'_{\hat{\rho}}\frac{\langle \mathbf{j}_{\mathrm{ni}}\cdot\mathbf{B}\rangle}{B_0} \quad (1)$$

- diffusion equation for the electron temperature:

$$\frac{3}{2}\frac{1}{(V'_{\hat{\rho}})^{5/3}}\left(\frac{\partial}{\partial t}-\frac{\dot{\Phi}_b}{2\Phi_b}\frac{\partial}{\partial\hat{\rho}}\hat{\rho}\right)\left[(V'_{\hat{\rho}})^{5/3}n_eT_e\right]=\frac{1}{V'_{\hat{\rho}}}\frac{\partial}{\partial\hat{\rho}}\left[\frac{g_1}{V'_{\hat{\rho}}}n_e\chi_e\frac{\partial T_e}{\partial\hat{\rho}}\right]+P_e \quad (2)$$

where $\mathbf{B}$ is the magnetic field, $F = RB_\phi$ is a poloidal current function, $\mathbf{j}_{\rm ni}$ is the non-inductive current density, χ_e is the electron heat diffusivity and the flux surface averaged geometrical parameters are: $V'_{\hat{\rho}} = \partial V/\partial\hat{\rho}$, $g_1 = \langle(\nabla V)^2\rangle$, $g_2 = \langle(\nabla V)^2/R^2\rangle$, $g_3 = \langle 1/R^2\rangle$.

Other kinetic parameters, like electron density n_e, ion temperature T_i and ion density n_i, are prescribed and either analytical profiles or experimental data can be used for their description during the simulation. Note that in Eqs. (1) and (2) the geometrical and kinetic profiles depend on time as well as: $V'_\rho(\rho,t)$, $n_e(\rho,t)$, etc. For compatibility with real-time execution [16], the full set of transport equations was reduced to these two equations. Such simplification is justified by the fact that the most important parameters for the plasma state description are electron temperature and poloidal flux. Indeed these quantities directly determine the transport properties, hence global confinement, and the plasma resistivity and current density profile, which provide the q profile time evolution depending on $T_e(\rho,t)$ as well. Moreover there is some level of uncertainty in the diffusion equation for the electron density, in particular to predict the particle sources like the wall recycling. Thus it was chosen to use experimental measurements for the electron density, which are much more reliable than a predicted value at this stage. In the first version of the model, described in [16],[25], the transport model used in RAPTOR has been constructed based on the fixed equilibrium assumption. It was supposed that magnetic field, geometry of flux surfaces and enclosed toroidal flux were fixed. This assumption is weaker than the condition of fixed Grad-Shafranov equilibrium, since, in RAPTOR, the poloidal flux profile $\psi(\rho)$ and therefore the current density j_{tor} and safety factor $q(\rho)$ can evolve in time. In [16] it was shown that the geometry profiles do not change a lot with Shafranov shift.

However the evolution of a plasma equilibrium geometry influences the plasma profiles and have to be taken into account in the case of simulations of entire discharges, where significant changes in the plasma state occur during ramp-up and ramp-down phases, in particular, including fast evolution of the plasma boundary. For this purpose, the simplified diffusion equations have been extended with the time-varying terms as stated in Eqs. (1)–(2). The parameters related to equilibrium geometry are defined through a linear interpolation of several equilibria corresponding to different time instants. The kinetic profiles $n_e(\rho,t)$, $T_i(\rho,t)$, $n_i(\rho,t)$ are now both space- and time-varying. The solution method used in RAPTOR is based on a finite-element approach which could be easily extended to include these new equations. See Appendix A for more details of the implementation of the time-varying terms in the code.

For the verification of the transport model extension, a benchmark with the ASTRA code has been performed. Data for an artificial TCV-like plasma geometry has been used. The Grad-Shafranov equation has been solved by ASTRA's internal prescribed-boundary equilibrium solver and then the equilibrium data has been processed by the CHEASE code to generate equilibrium geometry information as input for RAPTOR.

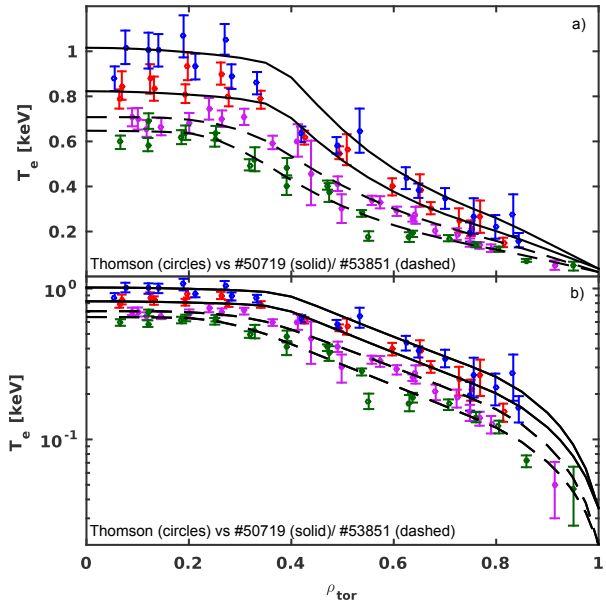

Figure 2. T_e ((a) linear plot, (b) log plot) simulated profiles by RAPTOR vs the experimental ones provided by Thomson measurements (circles) for the TCV shots #50719 (solid) and #53851 (dashed): ● – #50719 Ip=195 kA, ● – #50719 Ip=206 kA, ● – #53851 Ip=205 kA, ● – #53851 Ip=185 kA.

Both ASTRA and RAPTOR solve the diffusion equations for poloidal flux and electron temperature. Profiles for $n_e(\rho,t)$, $n_i(\rho,t)$, $T_i(\rho,t)$ have been defined as Gaussian profiles and fixed in time. Electron heat diffusivity $\chi_e(\rho,t)$ has been determined as a square function of a radial coordinate only. Figure 1 shows the results of the simulation in case when elongation of the plasma boundary has been increased from 1.2 to 1.5 in 800 ms. A decrease of the electron temperature and growth of the edge safety factor is expected and obtained with both codes which results are similar.

2.2. Gradient-based electron heat diffusivity model

In [22] it was shown that transport in the "core" (inside $\rho_V = 0.8$ for L-mode typically) and "pedestal" (ρ_V between 0.8 and 1.0) regions can be characterized by a constant logarithmic gradient and by a constant gradient correspondingly, even in L-mode. A normalized inverse scale length was defined as

$$\frac{R}{L_{Te}} = -\frac{R_0}{a}\frac{d\ln T_e}{d\rho_V} = \begin{cases} 0 & \text{for } \rho_V < \rho_{inv,T_e} \\ \dfrac{R_0}{a}\lambda_{Te} & \text{for } \rho_{inv,T_e} < \rho_V < \rho_{ped,T_e} \\ \dfrac{R_0}{a}\dfrac{\mu_{Te}}{T_e(\rho_V)} & \text{for } \rho_V > \rho_{ped,T_e} \end{cases} \quad (3)$$

Therefore the constants for the core and edge regions were defined as $\lambda_{T_e} = -{T_e}^{-1}\partial T_e/\partial(\rho/\rho_{edge})$ with the inverse scale length $R/L_{T_e} = R\lambda_{T_e}/\rho_{edge}$ and $\mu_{T_e} = -\partial T_e/\partial(\rho/\rho_{edge})$ for the electron temperature profile. It was demonstrated in [22] that,

for a wide range of scenarios, values of λ_σ ($\sigma = T_e,\ n_e$) are close to each other, whereas μ_σ reflects changes in thermal and particle transport and confinement. During this work the gradient-based transport model has been implemented into the RAPTOR code only for electron heat transport. It was first defined and used in [24]. The equation for the electron heat diffusivity is given by:

$$\chi_e = \underbrace{f\left(\frac{\rho-\rho_{inv}}{\delta\rho_{inv}}\right)\chi_{ST}}_{(a)} + f\left(\frac{\rho_{inv}-\rho}{\delta\rho_{inv}}\right)\frac{q_e}{V'\langle(\nabla\rho)^2\rangle n_e T_e} \tag{4}$$

$$\times\left[\underbrace{\frac{\lambda_{Te}}{\rho_{edge}}f\left(\frac{\rho-\rho_{ped}}{\delta\rho_{ped}}\right)}_{(b)} + \underbrace{\frac{\mu_{Te}}{T_e\rho_{edge}}f\left(\frac{\rho_{ped}-\rho}{\delta\rho_{ped}}\right)}_{(c)}\right]^{-1}$$

where ρ_{inv} is the sawtooth inversion radius which can be approximated by the $q = 1$ surface, ρ_{ped} is the pedestal position, $\delta\rho_{inv,ped}$ are the widths of the transition areas (center to core, core to edge), respectively using $f(x) = 1/(1+\exp(x))$ and $f \sim 1$ if $x < 0$ and $|x| \gg 1$ and $f \sim 0$ if $x > 0$ and $|x| \gg 1$. In this way the term (a) of Eq. (4) corresponds to the flat profile in the central region to take into account the influence of plasma sawtoothing on electron temperature profiles, the term (b) to the constant inverse scale length λ_{Te} in the core and the term (c) to the constant gradient μ_{Te} in the edge.

An essentially constant λ_{T_e} can be specified for a machine/scenario and then μ_{Te} is automatically adjusted to match the correct energy confinement time ratio for electrons $H_e = \tau_{E,e}/\tau_{scaling}$ [24], where $\tau_{scaling}$ is calculated with the $H_{98,y,2}$ scaling law [26] (but other scaling laws can be used). Figure 2 shows simulated and experimental radial profiles of the electron temperature for the TCV discharges #50719 and #53851. Simulations have been performed with fixed gradient for the core region $\lambda_{Te} = 3.2$ and $H_e = 0.4$. Figure 2 shows a very good agreement with the experimental profiles. In [24] at each time step the characteristic gradient μ_{Te} was calculated in the following way:

$$\mu_{Te}^{n} = \mu_{Te}^{n-1}\left\langle\frac{\tau_{scaling}H_e^{ref}}{\tau_{E,e}}\right\rangle_{time} \tag{5}$$

where ^{n} and $^{n-1}$ represent the values of the gradient at the current and previous time steps. If, for example, the estimated $H_e^{n-1} = \tau_{E,e}^{n-1}/\tau_{scaling}^{n-1}$ factor is lower than the prescribed one H_e^{ref}, μ_{Te} will be increased, hence the pedestal top as well, and as a result the whole electron temperature profile will be pushed up to match the desirable H_e value. In Eq. (5), averaging over time is performed on a characteristic time period (around 10-15 confinement times) to avoid spurious oscillations. This approach assumes slow variation of H_e during the simulation. In case of large and fast changes in the prescribed H_e, the effect on the electron temperature profiles is delayed because of the time averaging of μ_{Te}. For a correct simulation of L- to H-mode and H- to L-mode transitions, plasma profiles should react quite rapidly to changes in H_e. Therefore in this work the gradient μ_{Te} is calculated with the help of a feedforward and feedback

controller, implemented as part of the transport model, based on a ratio of simulated and prescribed values of H_e.

$$\mu_{Te}(t) = \underbrace{\mu^{ff}_{Te}(I_p(t), P_{tot}(t), n_{el}(t))}_{\text{feedforward}} + \underbrace{K_p \cdot e(t) + K_i \cdot \int^{\delta t} e(t)dt}_{\text{feedback}} \tag{6}$$

where K_p and K_i are the proportional and integrated gains for the PI controller, an error $e(t) = H_e^{ref} - H_e^{sim} = H_e^{ref} - \tau_{eE}/\tau_{scaling}$. Discussion of the controller and more details can be found in Appendix B.

Note that the transition between L- and H-modes is modelled here through a time evolution of the value of the pedestal position ρ_{ped} and the gradient in the edge region, μ_{Te}, which then result in a change of the whole profile to match the related expected thermal energy. This is effectively what happens experimentally. The only main part which is not specified by the model is the time rate of the LH or HL transition. We have used typical values observed in TCV and AUG, but a specific study would be required in order to better predict ITER cases for example.

2.3. The transport model validation

For the validation of the developed transport model, simulations of TCV and AUG plasmas have been performed. Experimental equilibria for the TCV simulations have been obtained with the LIUQE code. On the ASDEX Upgrade tokamak, the equilibrium code CLISTE is used for calculation of MHD equilibrium and the toroidal current density profile [27]. Also the integrated data analysis (IDA) [28] provides information about plasma equilibrium and profiles. The equilibria generated with the experimental codes have been re-calculated using the CHEASE code. Figures 3 and 4 show the experimental time traces of the plasma current I_p, input power P_{tot}, central electron density n_{e0}, electron temperature T_e and plasma internal inductance $l_i(3)$ and comparison with the RAPTOR simulation results for the TCV shot #55520 and the AUG shot #32546. Many other discharges have been tested and yield similar results. Typical values of the transport model parameters λ_{Te} and H_e have been defined using the experimental data for the TCV and AUG tokamaks, in particular, with T_e profiles constructed from Thomson measurements. This is an important advantage of this transport model which depends on parameters well-known experimentally. The number of equilibria required to characterize a plasma discharge depends on the plasma state time evolution, but at least three equilibria have to be taken for each of the ramp-up and ramp-down phases and a couple of extra equilibria for the flattop phase. The choice is easily made in order to follow well $I_p(t)$ and $\kappa(t)$ in particular with piecewise linear interpolations, as well as $\beta(t)$ and L-H-L transitions when needed. For the full simulations of TCV ohmic shot #55520 and AUG shot #32546, twelve and eleven CHEASE equilibria have been used respectively. Of course more equilibria can be used but it does not change the result. The time evolution of the total plasma current and of the radial profiles of the electron density have been taken from the experimental data. Ion temperature has been defined

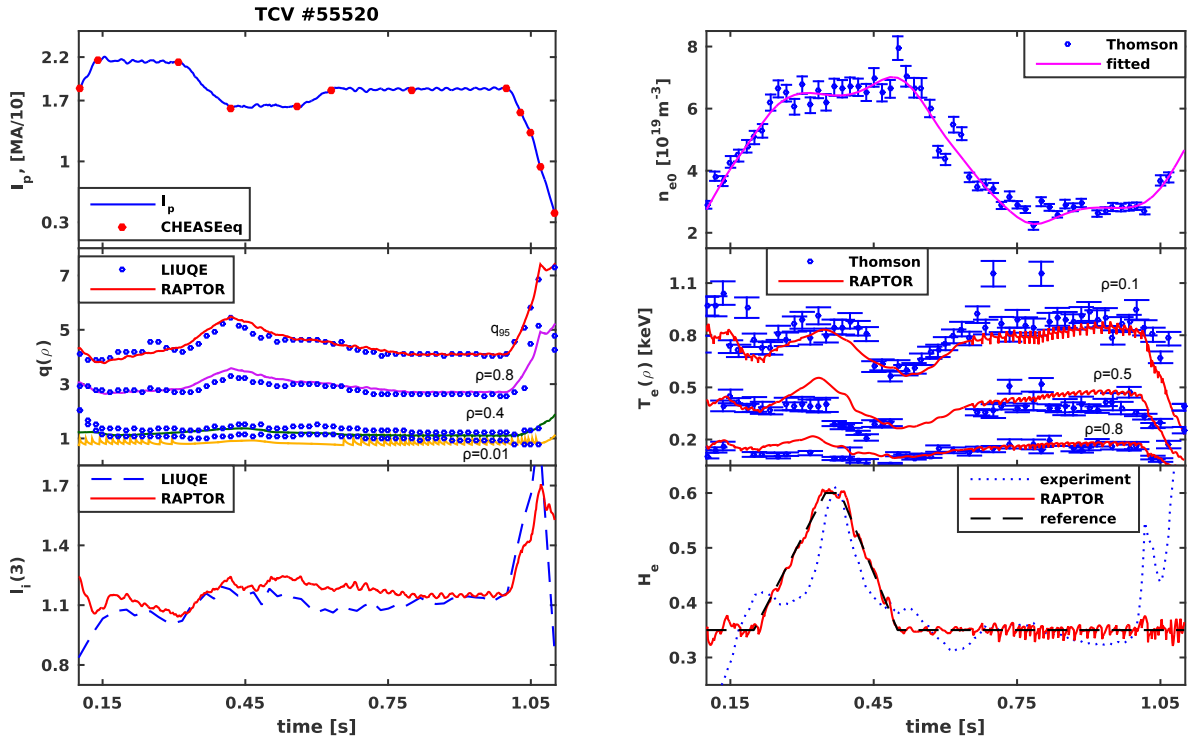

Figure 3. Comparison of RAPTOR simulation results and the plasma state profiles provided by the experimental database for the TCV shot #55520. Time traces of the following parameters are presented: plasma current I_p; safety factor q_{95} and $q(\rho_{tor})$ at $\rho_{tor} = [0.01,\ 0.4,\ 0.8]$; plasma internal inductance $l_i(3)$ provided by the RAPTOR and LIUQE codes; central electron density n_{e0} provided by Thomson measurements and fitted data used by RAPTOR; electron temperature $T_e(\rho_{tor})$ at $\rho_{tor} = [0.1,\ 0.5,\ 0.8]$ obtained with the RAPTOR code and Thomson measurements; H_e experimental, RAPTOR reference and simulated.

through a simple scaling of the experimental electron temperature profiles. Ion density has been scaled from the electron density profiles. The experimental Z_{eff} value is used, assuming a radially constant profile. For the simulation of the AUG shot, Gaussian radial profiles have been used for the description of the heating sources: NBI and ECH. We use an internal module for the RAPTOR code to simulate sawteething plasmas using the Porcelli crash criterium and Kadomtsev reconnection model [29, 30, 31].

For the TCV L-mode shot, the constant gradient for the core region λ_{Te} has been equal to 3.2. H_e-factor has been varied from 0.35 to 0.6 on the time interval [0.2 0.4] s to match experimental measurements and has been fixed at 0.35 for the rest.

For the AUG case L-H and H-L transitions have been specified from H_α measurements at 0.7 s and 8.55 s respectively. H_e-factor has been fixed at 0.2/0.4 for L-/H-mode. In the ramp-down phase, due to W accumulation and to match the experimental drop in electron temperature T_e, H_e-factor has been changed from 0.4 to 0.2 at 8.1 s instead of 8.55 s. Also to mimic flattening of the electron temperature

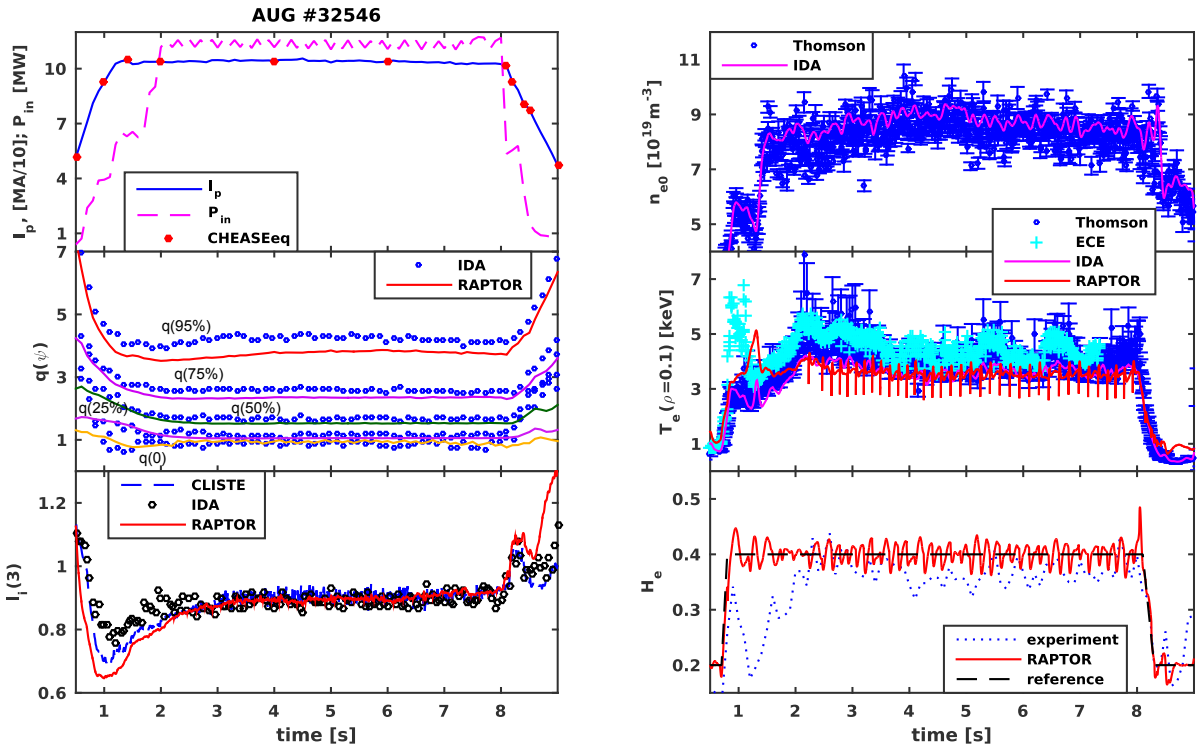

Figure 4. Comparison of RAPTOR simulation results and the plasma state profiles provided by the experimental database for the AUG shot #32546. Time traces of the following parameters are presented: plasma current I_p, total input power P_{in}; safety factor q_0 and $q(\psi)$ at 25%, 50%, 70%, 95% of flux surface; plasma internal inductance $l_i(3)$ provided by the RAPTOR, CLISTE, IDA codes; central electron density n_{e0} provided by Thomson measurements and fitted data from IDA used by RAPTOR; electron temperature $T_e(\rho_{tor} = 0.1)$ obtained with the RAPTOR code, IDA fitted profiles, Thomson and ECE measurements; H_e experimental, RAPTOR reference and simulated.

profiles on a time period [8.1 8.55] s, λ_{Te} has taken value of 1.5, whereas for the rest it has been equal to 3.0 for L-mode and 2.3 for H-mode.

From figures 3 and 4 it can be seen that the evolution of the central value of the simulated electron temperature is within the experimental error bars. The time evolution of the RAPTOR simulated safety factor q shows a good correspondence with the simulation results of the equilibrium reconstruction code LIUQE for TCV and IDA for AUG. Some difference can be mentioned for q_{95} in case of AUG simulation which is due by the fact is part by the fact that CHEASE does not consider the X-point configuration and thus assume the plasma is limited (finite q value at the edge). The simulated plasma internal inductance $l_i(3)$ follows the experimental one very well at the flat-top phase whereas during the ramp-down phase they are different but follow the same trends. The CLISTE code uses only the magnetic measurements to solve the Grad–Shafranov equilibrium equation and this is valid also for the TCV equilibrium

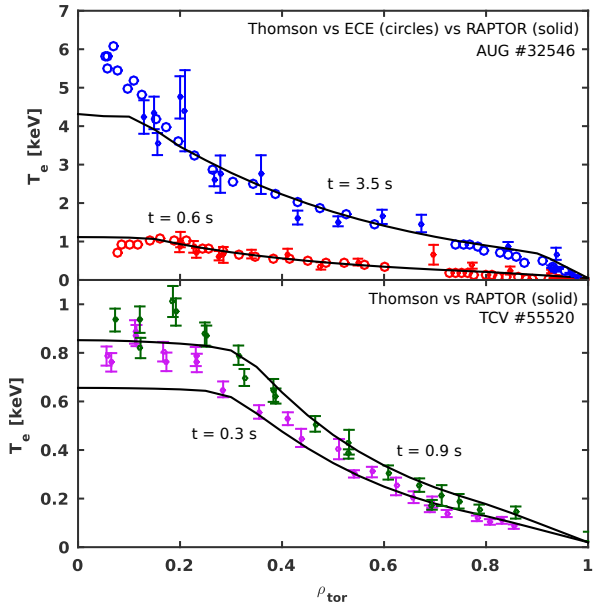

Figure 5. Radial profiles of electron temperature provided by RAPTOR (solid), Thomson (dots) and ECE (circles, for AUG shot) measurements for the TCV #55520 and AUG #32546 shots at two time slices for each shot.

reconstruction code LIUQE which was used to obtain $l_i(3)$ in Fig. 3. The disadvantage of using such codes for simulation of dynamic phases of a plasma discharge is the lack of information about currents generated in the vessel and surrounding structures which RAPTOR does not use either, and about the current density profile resistive diffusion which RAPTOR does compute. This can be a reason for the difference between the internal inductance simulated with RAPTOR and the one provided by the AUG/TCV databases. Since IDA takes the current diffusion into account, it might explain also why the l_i obtained through IDA is closer to RAPTOR than the result obtained by CLISTE. However the RAPTOR internal inductance increases still faster than IDA. It can be caused by the fact that IDA uses interpretative measured profiles of T_e and T_i, affected by high radiation and impurity accumulation during AUG ramp-down which RAPTOR does not take into account at this moment. A more systematic study to determine the realistic models should be performed, similarly to the ramp-up phase as has been done in [15], but it is out of the scope of this paper.

The electron temperature profiles at several time instants are demonstrated in Fig. 5. For AUG case, the pedestal area can be recognized for the H-mode case (for $t = 3.5$ s). For TCV discharges, we can use a typical value for the L-mode H_e factor of about 0.35-0.4. In the shot chosen in Fig 3, there is a transient improved confinement phase, between 0.2 s and 0.45 s. The reason is not clear and hard to determine, since many plasma parameters are changing (I_p, plasma shape, electron density n_e). However the present model can reliably recover the experimental behavior simply by adjusting one parameter H_e. In reality the improved confinement also leads to an improved λ_{T_e} (4.0

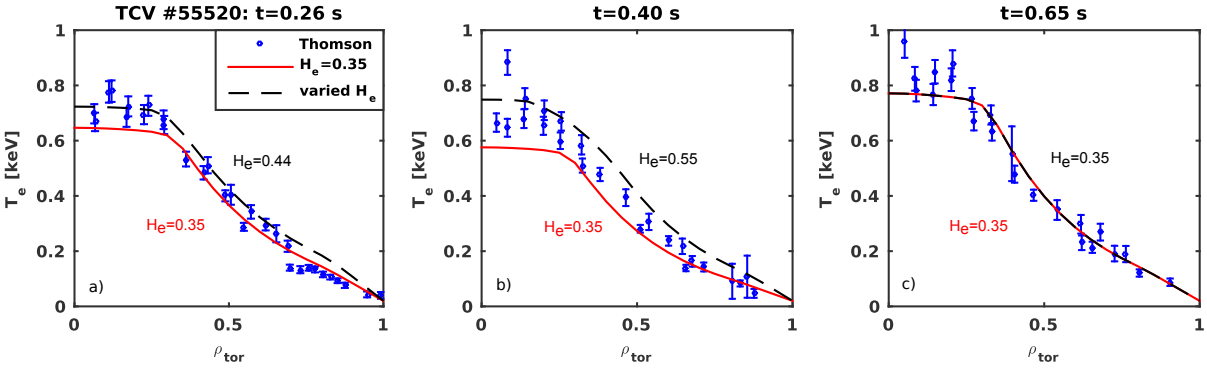

Figure 6. Comparison of Thomson measurements for TCV shot #55520 and RAPTOR simulation results in case of fixed $H_e = 0.35$ and varied H_e with $\lambda_{T_e} = 3.2$.

instead of 3.2) which we could use but we see in Fig 6(b) that adjusting H_e is sufficient. The global kinetic energy is easily known experimentally in real-time, thus this can be used to constrain the value of H_e. An exception is made for the fast particles contribution which needs to be obtained from off-line analysis. Note that at this stage RAPTOR assumes a given factor for T_i/T_e but an equation for T_i is being added to the model. On the other hand, if we simulate with RAPTOR-predictive, thus $H_e = 0.35$ fixed, we would observe the improved confinement phase with the difference between the predictive T_e profile and the measured one, see Fig 6. This is also an important information to be used for real-time scenario monitoring applications. Similarly, drop of confinement in the AUG ramp-down phase, which is still in H-mode, would be well identified by comparing the predictive T_e profile with the measured profiles, if the expected H_e(H-mode)= 0.4 is kept. This is one way to identify early, in real-time, the effect of impurity accumulation [32].

2.4. Simulation of the ramp-down phase

As it was mentioned above, non-disruptive termination is an important issue for ITER and safe scenarios have to be defined. Experimental study is one of the ways to analyze and to propose such scenarios. Comparison between machines allows to make conclusions on the most important characteristics of the termination phases and to extrapolate them for ITER cases [33]. The results shown in [33] also provide the main information required to analyze ramp-down phases and to compare between experiments, therefore to compare between experiments and simulations. Fig 7 shows the simulation results obtained with the RAPTOR code for two of the TCV discharges included to the multi-machine database, shot #53896 and #53897. We first see, similarly to Figs 3 and 4, that the plasma behavior is well reproduced by RAPTOR during ramp-down phases as well. Some differences are observed but are due in part to the different assumptions in the equilibrium reconstruction for transient plasma as discussed before. Nevertheless the differences are smaller than the variations observed

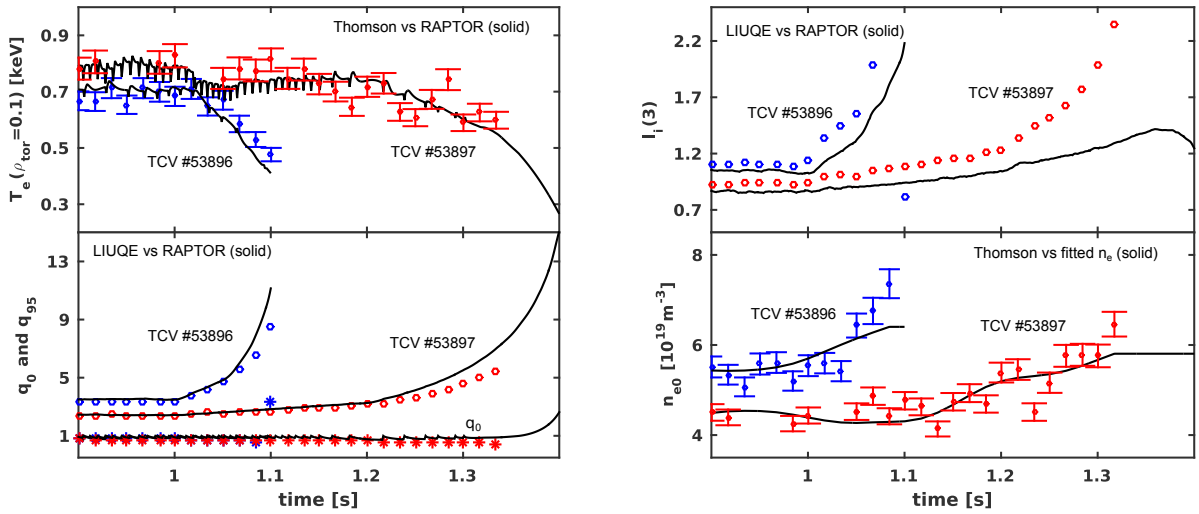

Figure 7. Comparison of RAPTOR simulation results and experimental measurements for TCV shots #53896 and #53897. Time evolution of the following parameters is presented: electron temperature $T_e(\rho_{tor} = 0.1)$ provided by the RAPTOR code (black solid) and Thomson measurements (dots); safety factor q_{95} and q_0, internal inductance $l_i(3)$ from the LIUQE (circles and stars) and RAPTOR codes; central electron density n_{e0} provided by Thomson measurements and fitted data used by RAPTOR.

in between experiments as shown in [33]. Therefore RAPTOR simulations, used to rapidly obtain the predicted time evolution for the q profile, l_i, etc during ramp-down are relevant for the experiment and for comparing simulations for different tokamaks.

3. Optimization of the ramp-down phase

The power sources and plasma current decrease during the termination phase causing fast changes in plasma state, supplemented by a strong coupling between physical parameters and technical requirements. One of the difficulties is the control of the plasma position. While the plasma current decreases, the internal inductance increases leading to a smaller efficiency of the vertical control system. If the internal inductance increases too quickly, so that the vertical control system can no longer stabilize the vertical instability, then the plasma will disrupt, typically with a vertical displacement event (VDE). VDEs are characterized as the most dangerous plasma events for ITER [34]. However a proper evolution of plasma shaping can reduce the growth of the internal inductance. Simulations of ITER plasma [8] and experiments on JET [11] have shown a strong effect of elongation on the internal inductance behavior. In addition to the vertical control, the radial position control has to be carefully implemented. A rate of change in a vertical magnetic field is limited by the rate of change in currents in the

poloidal field coils. By definition from [35] the vertical magnetic field is given by

$$B_v = \frac{\mu_0 I_P}{4\pi R}\left(\ln\left(\frac{8R}{a\kappa^{0.5}}\right) + \beta_p + 0.5 l_i(3) - 1.5\right) \tag{7}$$

Since it is a function of plasma current, internal inductance, elongation and β_{pol}, radial position control can be lost in case of rapid changes in the mentioned parameters. As a consequence, plasma position and shape control systems should be developed using knowledge of the evolution of the plasma profiles, i.e. integration of magnetic and kinetic control is required.

For a good performance, plasmas are generally operated in a high confinement mode (H-mode). During the termination phase, with the reduction of plasma current and mostly auxiliary power, it comes back to a low confinement mode (L-mode). Because of the transition from H- to L-mode, the plasma experiences a fast decrease of energy and pressure. In particular, it can lead to a significant drop in β_{pol}, faster than can be compensated by reducing the vertical field, therefore the plasma can make contact with the inner wall [36]. In [37] two scenarios of ITER plasma termination were demonstrated: with H-L transition and in pure H-mode. It was shown that the internal inductance in the first case stays lower, whereas the drop in β_{pol} was smaller in the second case. Therefore the moment of the H-L transition is quite important for a plasma position control and for a safe termination and it has to be specifically defined as will be shown in Sec 3.3. It should be mentioned that a fast growth of radiated power can also lead to H-L transition [26].

During plasma current ramp-down, the electron density has to be decreased to avoid disruptions caused by reaching the Greenwald density limit which depends on the plasma current. At the same time, the power load on the divertor has to be controlled. The dependence of the SOL and divertor parameters, like divertor power load, normalized neutral pressure and divertor neutral pressure, on the fueling scenario was shown in [38]. The core density can be controlled by pellets injection, whereas edge density is influenced by neutral gas puffing. In particular during the termination of an ITER plasma, transition from a regime with 80% of gas puff and 20% of core fueling to one with only pellet injection allows plasmas to stay attached with the normalized neutral pressure lower than one. However the control of density and its simulation is left for future studies. At this stage we assume that the density control system can provide the required line-averaged density. We only enforce a constraint such that it does not violate the Greenwald density limit or a fraction of it for safety margin. Note that this would lead to a constraint on the I_p ramp rate since the particle confinement time is relatively long up to 5-10 times greater than the energy confinement time [39].

The optimization procedure is described in Sec 3.1, while in Sec 3.2 and 3.3 ramp-down optimization results are presented for TCV and AUG respectively. A discussion on the optimization results can be found in Sec 3.4.

3.1. Formulation of the optimization problem

Plasma termination can be defined as successful if it is obtained without disruptions and is reproducible for a specific machine. From the physical point of view, it means that plasma parameters have to evolve within specific limits to keep the plasma non-disruptive. At the same time, technical requirements of a machine provide additional restrictions on the whole termination scenario.

An optimization of the plasma discharge can be defined as the determination of an optimal time evolution of the plasma parameters to lead a plasma to a desired state keeping it within the specific limits: physical ones (to avoid appearance of physical events which can lead to instabilities and then to disruptions) and technical ones (to be able to use the results of the optimization on a real machine). The parameters to optimize are related to those controllable inputs that have the capability of significantly changing the plasma state. Such actuators can act on a plasma either from inside (like the power of auxiliary heating and the noninductive current drive, particle injection) or from outside (like a gas flux, plasma shaping parameters). The profile of the poloidal flux is strongly influenced by the plasma current density (which depends on $T_e^{3/2}$ throughout the plasma conductivity), whereas the electron temperature profile depends mainly on power density profiles and geometrical quantities. The optimization goal is defined through the minimization of a cost function. The latter can include a wide range of plasma parameters: plasma current, plasma elongation, EC, NBI heating or current drive power, electron density, etc.

Simplified physical models are widely used for a ramp-up optimization in particular and feedback control design [40]. An optimization of the ramp-up phase of the plasma discharge with plasma current and EC heating as actuators has already been carried out with the RAPTOR code [25]. In particular, the simulation showed that a plasma current overshoot with early heating allows to get a V_{loop} radial profile close to the stationary state and a safety factor profile appropriate for a hybrid scenario operation. In the present work for ramp-down optimization, we use the same method as in [25].

Firstly, a set of parameters to be optimized has to be defined. In this work, and as a proof of principle, we optimize the evolution of the total plasma current I_p, plasma elongation (edge value) κ_{edge} and the time instant of the transition from H- to L-mode t_{HL}. The input vector of the time-dependent actuator trajectories $[I_p(t)\ \kappa_{edge}(t)\ t_{HL}]$ is parametrized by a vector containing a discrete set of scalar parameters. The trajectory $u_i(t)$ for the ith actuator is written as

$$u_i(t) = \sum_j^{n_i} P_{ij}(t) p_{i,j} \tag{8}$$

where $P_{ij}(t)$ is a scalar function of time (piecewise linear or piecewise constant function with a finite support and maximum $P_{ij}(t) = 1$), the scalar $p_{i,j}$ gives the weight of the associated function, n_i is the number of parameters which define the ith actuator trajectory. More details can be found in [25].

A cost function has to be minimized during the optimization. Here it has been

defined as a sum of the time integrals of the total plasma current I_p and of the total input power P_{tot}:

$$J = \nu_{I_p} \int_{t_{RD}}^{t_{end}} I_p(t)dt + \nu_{P_{tot}} \int_{t_{RD}}^{t_{end}} P_{tot}(t)dt \tag{9}$$

Here we integrate over the termination phase, i.e. from the start of I_p ramp-down t_{RD} to the end of a plasma shot t_{end}. The optimization goal is to decrease I_p and input power as fast as possible to reduce the amount of energy stored in the plasma in order to reduce the risks related to a disruption during the ramp-down phase [41, 42]. Other options, like a time integral of the plasma thermal energy or I_p^2, can be easily added to the cost function.

As it was mentioned, there are plenty of physical and technical issues important for a safe termination. In this first study, it is not possible to take all of them into account during the optimization, therefore the most crucial ones have to be defined. However we present here a model which can easily be updated to include new goals in the cost function and new constraints. The constraints used in the present work can be divided into physical and technical ones:

- physical:
  - line averaged electron density n_{el} lower than 90% of $n_G = I_p(t)/\pi a^2$ (Greenwald density limit);
  - safety factor q_{95} greater than q_{95} at the beginning of the ramp-down phase;
  - β_N below a certain limit (MHD limit);
  - other physical constraints;
- technical:
  - ramp-down rate of the plasma current dI_p/dt;
  - ramp-down rate of the plasma elongation $d\kappa/dt$;
  - limit plasma internal inductance $l_i(3)$ for vertical position control;
  - limit the maximum rate of change of the vertical magnetic field dB_v/dt for radial position control;
  - other technical constraints specific for a machine.

Here upper and lower boundaries for the elements of the vector p (Eq. (8)) as well as limits on ramp rates (except on t_{HL}) are specified through linear inequality constraints.

$$A_{ineq} p \leq b_{ineq} \tag{10}$$

A constraint on the highest/lowest value of any other parameter ($\beta_N(t), l_i(3)(\rho, t)$, etc) can be specified in the same way as has been described in [25].

As it was mentioned in Sec. 2.1 RAPTOR uses prescribed CHEASE equilibria taken at several time instants at the termination phase. The geometrical quantities defined in Eqs. 1-2 are automatically extracted from CHEASE equilibria. During the optimization of the plasma elongation κ, these profiles are scaled proportionally to κ. We have verified that the optimized trajectory is very similar when we recompute the

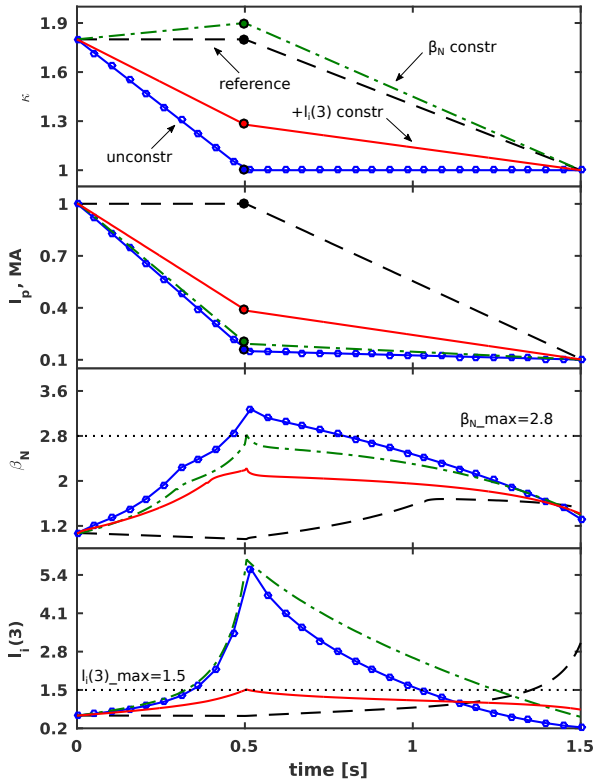

Figure 8. A simple ramp-down optimization for AUG-like plasma. Time evolution of the plasma boundary elongation κ, plasma current I_p, normalized beta β_N and plasma internal inductance $l_i(3)$ are demonstrated for the reference case (black dashed), unconstrained optimization (blue solid with circles), optimization with the constraint on β_N (green dot-dashed), optimization with constraints on β_N and $l_i(3)$ (red solid).

geometrical profiles with CHEASE solution using the optimized elongation and the RAPTOR pressure and current density profiles.

Figure 8 shows a simple ramp-down optimization for AUG-like plasma with a set of constraints imposed on the ramp-down rate of the plasma current ($dI_p/dt \geq -1.9$ [MA/s]), normalized beta ($\beta_N \leq 2.7$) and plasma internal inductance ($l_i(3) \leq 1.2$). The reference trajectories of the plasma current I_p and boundary elongation κ to be optimized are marked as dashed lines. The optimization point is at $t = 0.5$ s, the initial and final values are fixed and define maximum and minimum values of I_p and κ. In case of unconstrained optimization, I_p and κ take the lowest allowed values at $t = 0.5$ s (blue line with circles on figure 8), thus the cost function is minimized. To keep I_p lower while adding the constraint on β_N (dot-dashed green line), elongation has to be increased in comparison to the reference case. In case of optimization with constraints on β_N and $l_i(3)$ faster current ramp-down can be reached with faster decrease in the plasma elongation κ. The constraint on internal plasma inductance is the most stringent one and its behavior is mostly defined by the time evolution of the plasma elongation and, consequently, the plasma surface. Here, as a simple example, optimization of I_p and κ has been performed only at one time instant $t = 0.5$ s, whereas a set of optimization

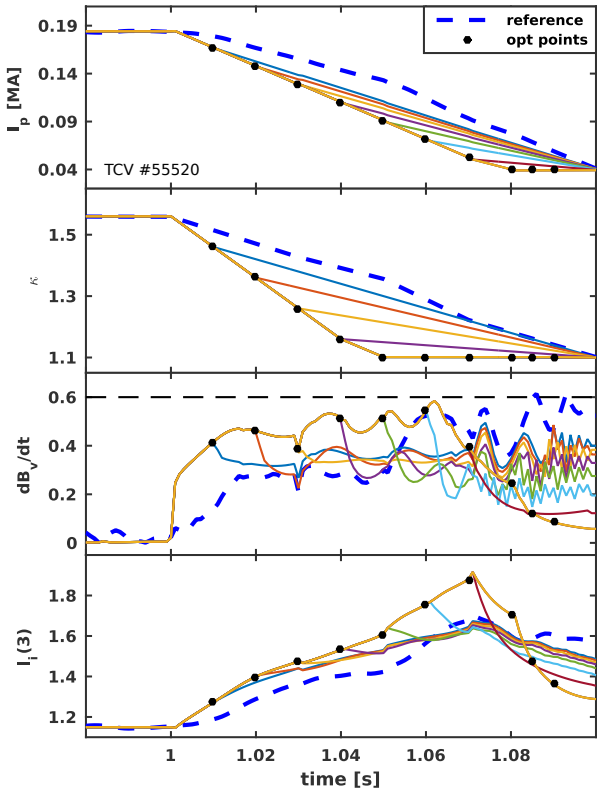

Figure 9. Ramp-down optimization for the TCV shot #55520 (color online). Time traces for plasma current I_p, plasma boundary elongation κ, rate of change in vertical magnetic field dB_v/dt and plasma internal inductance $l_i(3)$ are presented for the reference case (blue dashed) and various optimized trajectories (colorful solid) with the optimization points (black dots).

points has to be used to obtain an optimal trajectory which leads to a true minimum of the cost function within the required constraints.

In contrast with [25], where the search direction of the optimal solution is defined by using analytical gradients of the cost function, here we use numerical gradients calculated by finite differences within the optimization algorithm. The reason is in the difficulty of an analytical description of the plasma state gradients in terms of plasma geometry and confinement state. In [25] one could make use of the analytical gradients that came as a by-product of the implicit time-solver of the PDE. In this work, however, we require gradients with respect to geometric terms such as g_2, g_3... which are not calculated by the PDE solver. The main disadvantage of finite differences usage is an increase of the CPU time required for an optimal solution search. Nevertheless results can still be obtained within a reasonable amount of time thanks to the high speed of the RAPTOR solver, typically about 1 hour on one cpu for the case shown in Fig 8.

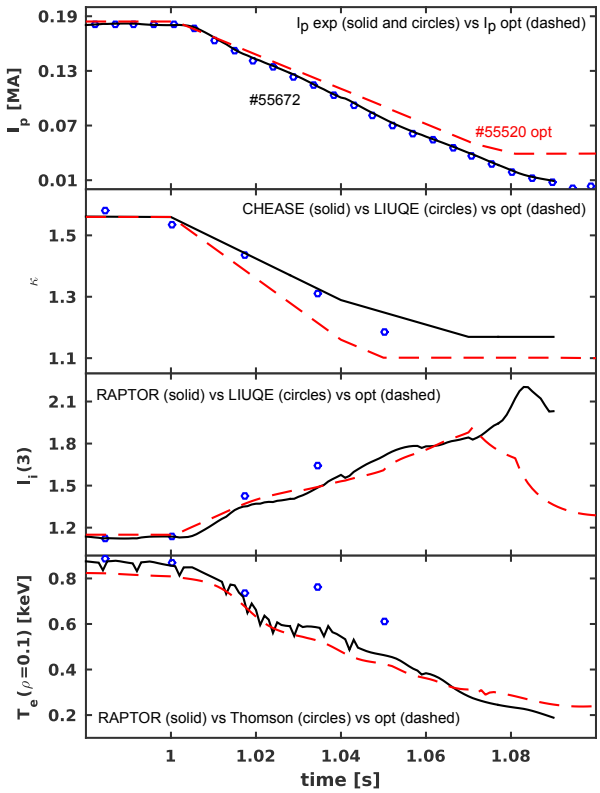

Figure 10. Time traces of I_p, κ, $l_i(3)$ and $T_e(\rho = 0.1)$ for the optimized TCV shot #55520 (dashed red), from the experimental data base for the TCV shot #55672 (blue circles) and RAPTOR simulation of #55672 (black solid).

3.2. Ramp-down optimization for TCV

Optimization of the plasma current I_p and elongation κ for the TCV shot #55520 has been performed. The transport parameters λ_{Te} and H_e have been fixed at the L-mode values, 3.2 and 0.35 correspondingly. The cost function is defined according to Eq. (9) with $\nu_{I_p} = 1$ and $\nu_{P_{tot}} = 0$. The physical constraints have been imposed on the safety factor $q_{95} \geq 3.3$ (minimum value for the reference case) and on the rate of change of vertical magnetic field $dB_v/dt \leq 0.6$ [T/s]. The technical constraints on ramp-down rate of I_p and κ have been obtained from the experimental database, based on various terminations of TCV plasmas and have been set to -1.9 [MA/s] and $-10\ s^{-1}$. Plasma current and elongation trajectories have been optimized in series of 10 points: starting from the reference trajectories, I_p and κ have been optimized first at $t = 1.01$ s, then starting from the optimized trajectory I_p and κ have been optimized at $t = [1.01,\ 1.02]$ s and so on up to the final set of 10 optimization points. The reference and optimized (with number of optimization points varied from 1 to 10) trajectories of I_p, κ, B_v and $l_i(3)$ are shown in Fig. 9. Shot #55520 was ohmic L-mode and has been terminated down to $I_p = 40$ kA. Optimization has shown that faster ramp-down in I_p can be performed while keeping B_v at a safe level, but κ has to be decreased faster than the reference. Note

that increasing the number of optimization points will not decrease the cost function anymore and the set of 5 optimization points $t = [1.01,\ 1.04,\ 1.05,\ 1.07,\ 1.08]$ s is sufficient to get the same optimized trajectory. Note that local minima might exist beyond the optimization procedure. We have checked that the optimized trajectory is the same if the sequence of optimization points is taken in a different order.

A fast ramp-down of both Ip and kappa has been successfully tested on the TCV tokamak, following the present simulated results. In Fig. 10 optimized trajectories for the TCV shot #55520, experimental time traces and RAPTOR simulations for the TCV shot #55672 are presented. For #55672 the time traces for the plasma current I_p and plasma elongation κ have been programmed according to the optimized trajectories of #55520 following the dark yellow time traces marked with black dots on Fig 9. The RAPTOR transport model for #55672 was the same as for #55520. As it can be seen from Fig. 10, a fast ramp-down in I_p, even with a slightly slower decrease in κ than expected, allows to have a non-disruptive termination. Note that the predicted (from the optimization) and the simulated time evolution of l_i and T_e are very similar to the TCV results, validating our model and procedure. Further experimental tests are required to check capabilities of the shaping control system.

3.3. Ramp-down optimization for AUG

The same kind of optimization procedure has been done starting from the ramp-down of the AUG shot #33589. The transport parameters λ_{Te} and H_e have been varied from the H- to L-mode values, 2.3/3.0 and 0.2/0.4 correspondingly. The maximum plasma current ramp-down rate is set to 0.7 [MA/s]. The additional physical constraints have been imposed on the internal plasma inductance $l_i(3) \leq 1.4$ (maximum value for the reference case), normalized beta $\beta_N \leq 1.1$ (maximum value for the reference case), safety factor $q_{95} \geq 4.4$ (minimum value for the reference case) and on electron density to keep it within Greenwald density limit. The reference trajectories are shown with the blue dot-dashed lines on Fig. 11 (color online).

First, plasma current I_p and plasma boundary elongation κ have been optimized with 13 points with $\nu_{I_p} = 1$ and $\nu_{P_{tot}} = 0$ for the cost function defined in Eq. (9) (dashed green lines on Fig. 11). The input power and time of HL transition is kept as in the reference. It shows that, with a proper reduction of the plasma elongation, plasma current ramp-down can be done faster then the reference while keeping the internal plasma inductance at a safe level and other parameters within the required limits.

Then the instant of the H- to L-mode transition t_{HL} has been added to the set of optimization parameters. Here the H-L transition has been defined as a time instant when $P_{NBI} \leq P_{LH}$ where P_{LH} represents a power level required for LH transition and has been calculated according to [43]. In this optimization example, the cost function is defined as Eq. (9) with $\nu_{I_p} = 0.5$ and $\nu_{P_{tot}} = 0.5$, i.e. the goal of the optimization is to minimize both plasma current and input power. The reference value of t_{HL} is 6.26 s, the optimized value is 6.05 s. Slightly different time evolution of elongation and early drop

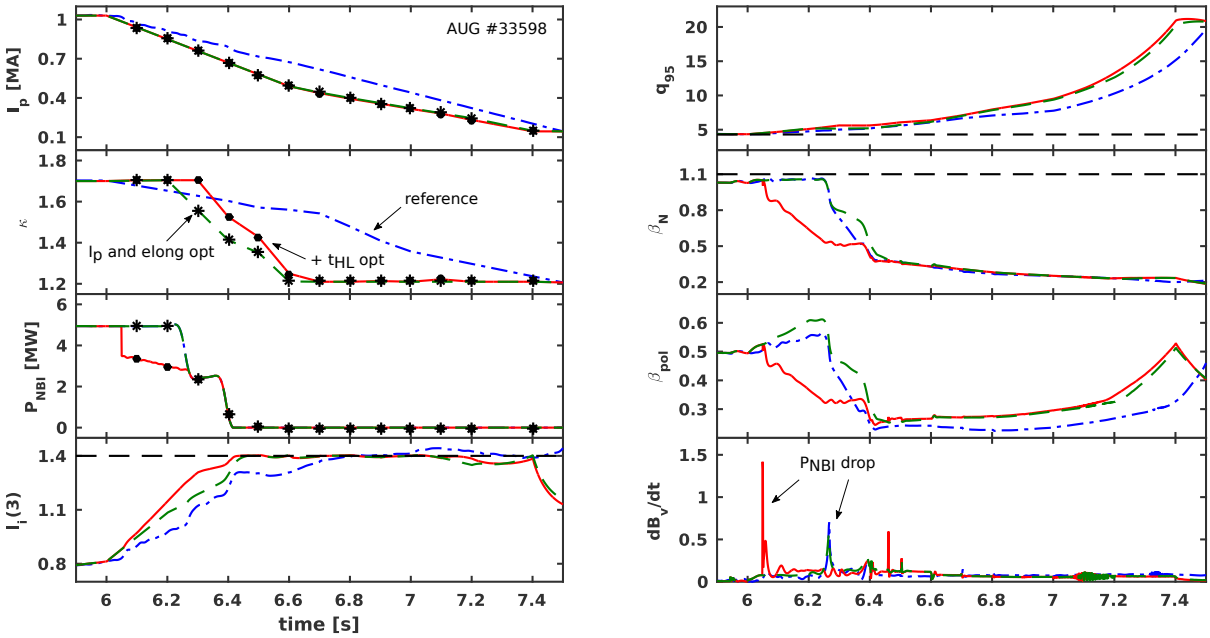

Figure 11. Ramp-down optimization for the AUG shot #33589. There are presented the reference trajectories (blue dot-dashed), results of optimization of I_p and κ time evolution (green dashed), results of optimization of t_{HL} in addition to two other optimization parameters (red solid). Time traces for the following parameters are shown: plasma current I_p, plasma boundary elongation κ, NBI power P_{NBI}, plasma internal inductance $l_i(3)$ and 1.4 limit, safety factor q_{95} and 4.4 limit, normalized beta β_N and 1.1 limit, poloidal beta β_{pol}, rate of change in vertical magnetic filed dB_v/dt. Optimization points are marked by the black dots (I_p and κ optimization) and stars (I_p, κ and T_{HL} optimization).

of the input power give the same time evolution for plasma current (which is limited by the allowed ramp-down rate) and keep plasma inductance within the required limit. Also, the early H-L transition case yields a smaller drop in poloidal beta β_{pol} than in the reference case, which can be important for MHD stability and radial position control. It also helps to decrease the density faster and to avoid density limit while decreasing I_p. The set of the optimization points can be limited by the first 7 points (from 6.1 s to 6.7 s) and the last one (7.4 s) to get the same optimized trajectories for I_p, κ and t_{HL}. At the same time there is no limit on the rate of change in vertical magnetic field dB_v/dt and as can be seen from Fig. 11, an earlier drop in NBI power produces higher peaking of dB_v/dt. Further analysis of experimental data and the machine characteristics is required for understanding and specifying a relevant limit for dB_v/dt (i.e disruptions caused by loss of radial position control) for AUG simulations.

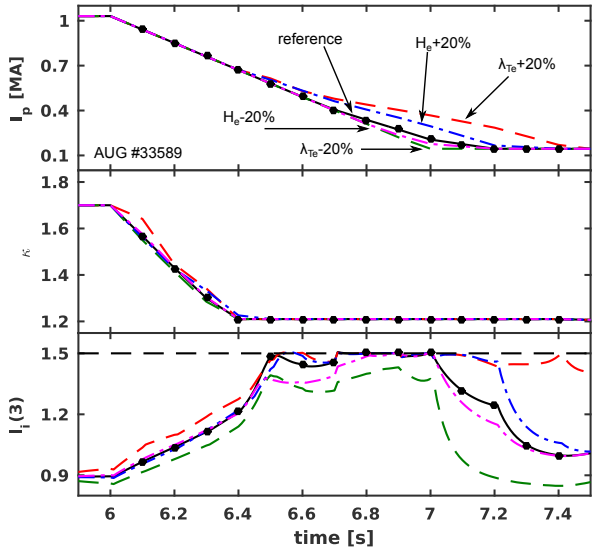

Figure 12. Test of the sensitivity of the I_p and κ optimized trajectories to the transport model parameters λ_{Te} and H_e. The optimized trajectories are obtained with the reference transport model (black solid) from Sec. 3.3, $\lambda_{Te} + 20\%$ (red dashed), $\lambda_{Te} - 20\%$ (green dashed), $H_e + 20\%$ (blue dot-dashed) and $H_e - 20\%$ (magenta dot-dashed). The optimization points are marked by the black dots (color online).

3.4. Ramp-down optimization discussion

These TCV and AUG demonstration cases show that there is a room for optimizing plasma ramp-down scenarios and that the dynamic dependencies make it difficult to "guess" the best trajectory. On the other hand, optimizing the trajectories as proposed here allow to easily get the correct balance between I_p reduction, κ reduction and H-L transition to control l_i, dB_v/dt and β_{pol}. For example the first part can be understood since decreasing I_p at the same rate as the plasma surface will tend to keep the q profile self-similar, hence will not increase l_i significantly. Of course, the resulting optimized trajectory can be tested in more complex codes like DINA-CRONOS. In this way an overall accurate optimization can be obtained faster.

Another important issue requiring a careful study is related to the sensitivity of the optimized trajectories to the transport model. In particular, increased core gradient λ_{Te} and/or H_e factor lead to higher internal inductance l_i because the electron temperature profile and, as a consequence, the current density profile become more peaked. If l_i is used as a constraint for the I_p optimization then the plasma current I_p optimized with higher λ_{Te} decreases slower to keep l_i within the required limit. For the sensitivity test, a set of optimizations on the plasma current I_p and the plasma boundary elongation κ for the AUG shot #33589 with varied transport model parameters has been performed (Fig. 12). To compare with the reference transport model used in Sec. 3.3 with $\lambda_{Te} = 2.3/3.0$ and $H_e = 0.2/0.4$ for the H- and L-modes respectively, we vary λ_{Te} and H_e by $\pm 20\%$. To analyze the influence on the plasma elongation κ in a meaningful way it has also

been included into the cost function with 0.2 weight, i.e. according to Eq. 9:

$$J = 0.8 \int_{t_{RD}}^{t_{end}} I_p(t)dt + 0.2 \int_{t_{RD}}^{t_{end}} \kappa_{edge}(t)dt \tag{11}$$

The optimization points are defined on the interval from 6.1 to 7.4 with 0.1 s step, i.e. 14 points in total. Only two constraints are defined for this test: $dI_p/dt \geq -0.9$ [MA/s] and $l_i(3) \leq 1.5$. As it can be seen from Fig. 12, increased transport parameters λ_{Te} and H_e lead to slower current ramp-down as it was expected. Whereas in case of decreased λ_{Te} and H_e the optimized trajectories for I_p are constrained mainly by the limit on dI_p/dt.

Fig. 12 shows that the optimized trajectory is not too sensitive to the transport model in the sense that the maximum difference in the final cost function values is only 10%. There is no big change in the optimized trajectories for κ. First stage in the plasma current I_p ramp-down (from 6 s to 6.4 s) is the same for all tests. This stage is the most important for the vertical stability since the plasma evolves from high (1.7) to low (1.2) elongation. The plasma internal inductance l_i increases rapidly but stays within the required limit for all transport models due to κ decrease. In this phase, l_i depends mostly on "edge" conditions namely κ and I_p rate. During the second stage (from 6.4 s to 7.5 s) κ stays constant and I_p trajectories depend on the transport model parameters since l_i trajectories are defined by I_p ramp-down rate and core profiles. This why the optimized trajectory for $\lambda_{Te} + 20\%$ deviates and leads to a slower ramp-down rate for I_p. We have also checked that if we use $\lambda_{Te} \pm 20\%$ for simulations with the reference optimized trajectories for κ and I_p we obtain about 20% difference in l_i $(1.3 - 1.8)$. Note however that the main difference appears when κ has been reduced to minimum and therefore the plasma might be expected vertically stable for l_i higher than the optimization limit. For further optimization studies the limit on the internal plasma inductance l_i can be defined as a complex parameter depending on the plasma elongation κ. It should be mentioned that additional constraints can better demonstrate effects of transport model parameters on the optimized plasma elongation. For example, β_N is proportional to the volume averaged pressure, therefore it depends on the plasma energy and plasma volume. Increased λ_{Te} leads to higher thermal energy and, to keep β_N within the required limit, the optimization algorithm can ask for a higher volume, i.e. higher kappa. Such sensitivity study can be very useful for real-time control, providing not just a trajectory for a plasma actuator but an area where a plasma is known to be within the physical/technical limits for a wide range of transport parameters. For this purpose one can develop a real-time optimal reference generation algorithm that can choose the best reference trajectory out of a pre-computed set of optimal trajectories for assumed levels of transport (and other parameters).

4. Conclusion

The present work has been focused on simulation and optimization of termination phase of plasma discharges. Appropriate transport models have been developed, and

successfully applied to TCV and AUG plasmas, and then used for numerical study and optimization of ramp-down phases. Simulations have been performed with the RAPTOR code which is a fast simulator of the poloidal flux and the electron temperature profiles. To take into account the time evolution of plasma geometry during ramp-up and ramp-down phases, its transport model has been extended to include the time-varying terms. Also a new adhoc model for electron heat transport has been implemented into the code, updated from the one proposed in [24]. While in the present work this transport model is used for offline simulations, it is also rather promising for the plasma real-time control. We leave it for further studies. The numerical simulations have been successfully verified via the comparison with numerical results of the ASTRA code (Fig. 1) and with the experimental data for full TCV (Fig. 3) and AUG discharges (Fig. 4). The presented developments allow for a fast and relatively accurate replication of the current density and temperature profiles time evolution during entire plasma discharges with L/H- and H/L-modes transitions. It is planned to continue development of the RAPTOR transport model, in particular to add the diffusion equations for electron density and ion temperature, as well as simplified models for impurity transport.

A new general method for systematic ramp-down study and optimization has been proposed. Numerical optimization of the ramp-down phases of TCV (Fig. 9) and AUG discharges (Fig. 11) shows that proper time evolution of plasma elongation and specification of the time instant of the H- to L-mode transition can help to control radial and vertical position of a plasma discharge, through a control of l_i and β_{pol}, and allow for fast I_p ramp-down. Preliminary experimental tests of the optimized trajectories for the TCV L-mode case have been successful. Further experiments on TCV and AUG are required for a full demonstration of the optimization procedure and to the model development (improving cost functions and technical and physical limits). It should be mentioned that the influence of radiated power is not considered in this work, but is an important issue and will be included to the optimization procedure later. In particular its effect on the duration of H-mode and a transient phase has to be investigated. The future research directions of ramp-down optimization are related to adding new physical and technical constraints and further study of its sensitivity to the transport model parameters. However the results and proof-of-principle presented here demonstrate the capabilities of the present method and show already interesting directions for imposing termination strategies.

Acknowledgments

This work was supported in part by the Swiss National Science Foundation. This work has been carried out within the framework of the EUROfusion Consortium and has received funding from the Euratom research and training program 2014-2018 under grant agreement No 633053. The views and opinions expressed herein do not necessarily reflect those of the European Commission. The views and opinions expressed herein do not necessarily reflect those of ITER Organization.

Appendix A. Numerical implementation

In the RAPTOR code, the system of ODEs (1)–(2) is solved by using the method of finite elements [16]. As in [16], the solution of an inhomogeneous equation of the form

$$m(\rho,t)\frac{\partial y}{\partial t} = \frac{\partial}{\partial \rho}\left[g(\rho,t)\frac{\partial y}{\partial \rho}\right] + k(\rho)j(\rho,t) \tag{12}$$

can be written as $y(\rho,t) \approx \sum_{\alpha=1}^{n_{sp}} \hat{y}_\alpha(t)\Lambda_\alpha(\rho)$. Here Λ_α are the finite element basis functions.

In order to easily use the finite element method, the terms of Eq. (1) have to be regrouped to eliminate the term in front of the second order derivative, since an integration by part is used later:

$$m_\psi \frac{\partial \psi}{\partial t} = a_\psi \frac{\partial \psi}{\partial \hat{\rho}} + \frac{\partial}{\partial \hat{\rho}} d_\psi \frac{\partial \psi}{\partial \hat{\rho}} + s_\psi \tag{13}$$

with

$$\begin{aligned}
m_\psi &= 16\pi^2 \mu_0 \hat{\rho} \frac{\Phi_b^2 \sigma_\parallel}{F^2} \\
a_\psi &= 8\pi^2 \mu_0 \dot{\Phi}_b \Phi_b \frac{\sigma_\parallel \hat{\rho}^2}{F^2} \\
d_\psi &= \frac{g_2 g_3}{\hat{\rho}} \\
s_\psi &= -8\pi^2 \mu_0 \Phi_b \frac{V'_{\hat{\rho}}}{F^2} \langle \mathbf{j}_{\mathrm{ni}} \cdot \mathbf{B} \rangle
\end{aligned}$$

Note that with respect to [25] a new term a_ψ has been added to reflect the time dependence of the toroidal enclosed flux Φ.

The same procedure has been applied to Eq. (2) resulting in an equation:

$$m_{T_e} \frac{\partial T_e}{\partial t} = a_{T_e} \frac{\partial T_e}{\partial \hat{\rho}} + \frac{\partial}{\partial \hat{\rho}} d_{T_e} \frac{\partial T_e}{\partial \hat{\rho}} + h_{T_e} T_e + s_{T_e} \tag{14}$$

with

$$\begin{aligned}
m_{T_e} &= \frac{3}{2} V'_{\hat{\rho}} n_e \\
a_{T_e} &= \frac{3}{2} \hat{\rho} n_e V'_{\hat{\rho}} \frac{\dot{\Phi}_b}{2\Phi_b} \\
d_{T_e} &= \frac{g_1}{V'_{\hat{\rho}}} n_e \chi_e \\
h_{T_e} &= -\frac{5}{2} n_e \frac{\partial V'_{\hat{\rho}}}{\partial t} - \frac{3}{2} V'_{\hat{\rho}} \frac{\partial n_e}{\partial t} \\
&+ \frac{3}{2} \frac{\dot{\Phi}_b}{2\Phi_b} \left(V'_{\hat{\rho}} n_e + \frac{5}{3} \hat{\rho} n_e \frac{\partial V'_{\hat{\rho}}}{\partial \hat{\rho}} + \hat{\rho} V'_{\hat{\rho}} \frac{\partial n_e}{\partial \hat{\rho}} \right) \\
s_{T_e} &= V'_{\hat{\rho}} P_e
\end{aligned} \tag{15}$$

As in the equation for toroidal flux, there is the term a_{T_e} which reflects changes caused by the time-varying enclosed toroidal flux $\dot{\Phi}_b$. Also a new term h_{T_e} has been

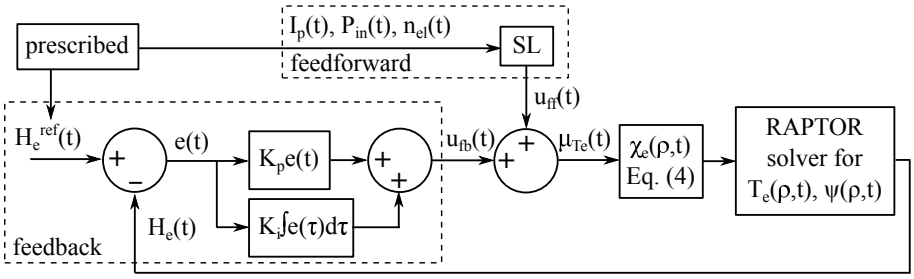

Figure 13. The block diagram for the μ_{Te} controller as a combination of PI feedback control with an error equal to $H_e^{ref} - H_e$ and feedforward control based on prescribed $I_p(t)$, $P_{in}(t)$ and $n_{el}(t)$.

defined to take into account the influence of the time evolution of the electron density and plasma volume.

For the T_e equation the weak form, after projection on Λ_b and integration by parts is

$$\sum_{\alpha=1}^{n_{sp}} \frac{\mathrm{d}\hat{y}_\alpha(t)}{\mathrm{d}t} \int_0^1 m_{T_e} \Lambda_\beta \Lambda_\alpha \mathrm{d}\hat{\rho} = \sum_{\alpha=1}^{n_{sp}} \hat{y}_\alpha \int_0^1 a_{T_e} \Lambda_\beta \frac{\partial \Lambda_\alpha}{\partial \hat{\rho}} \mathrm{d}\hat{\rho} \tag{16}$$
$$- \sum_{\alpha=1}^{n_{sp}} \hat{y}_\alpha \int_0^1 d_{T_e} \frac{\partial \Lambda_\beta}{\partial \hat{\rho}} \frac{\partial \Lambda_\alpha}{\partial \hat{\rho}} \mathrm{d}\hat{\rho} + \left[d_{T_e} \Lambda_\beta \frac{\partial \psi}{\partial \hat{\rho}} \right]_0^1 + \sum_{\alpha=1}^{n_{sp}} \hat{z}_\alpha \int_0^1 h_{T_e} \Lambda_\beta \Lambda_\alpha \mathrm{d}\hat{\rho} + \int_0^1 \Lambda_\beta s_{T_e} \mathrm{d}\hat{\rho}$$

which gives the matrix form

$$\mathbf{M_{T_e}} \frac{\mathrm{d}\hat{\psi}}{\mathrm{d}t} = (-\mathbf{D}_{T_e} + \mathbf{A}_{T_e} + \mathbf{H}_{T_e}) \hat{T}_e + \mathbf{l} + \mathbf{s} \tag{17}$$

The boundary term $\mathbf{l}$ contains only the last element

$$l = d_{T_e} \Lambda_\beta \frac{\partial T_e}{\partial \hat{\rho}} \Big]_{\hat{\rho}=1} = \frac{g_1}{V'_{\hat{\rho}}} n_e \chi_e \frac{\partial T_e}{\partial \hat{\rho}} \Big]_{\hat{\rho}=1} \tag{18}$$

Appendix B

The controller for the value of μ_{T_e} (Eq. 6) allows to get good predictive results even with fast L-H and H-L transition (Fig. 4). The block diagram of the controller is presented in Fig 13. For an error estimation as part of PI-feedback control, the prescribed $H_e(t)$ is required. For feedforward control, we use a simple scaling law based on prescribed plasma current $I_p(t)$, total input power $P_{in}(t)$ and line-averaged electron density $n_{el}(t)$. The transport parameter μ_{Te} obtained after the combination of feedforward and feedback outputs is used for $\chi_e(\rho)$ calculation and to solve for the electron temperature $T_e(\rho)$ profile. The H_e factor, based on this $T_e(\rho)$, is used for feedback control at the next step.

It is helped if a reasonable feedforward value μ_{Te}^{ff} can be provided. From the definition of the inverse scalelength R/L_{Te} (3), the constant gradient for the "pedestal"

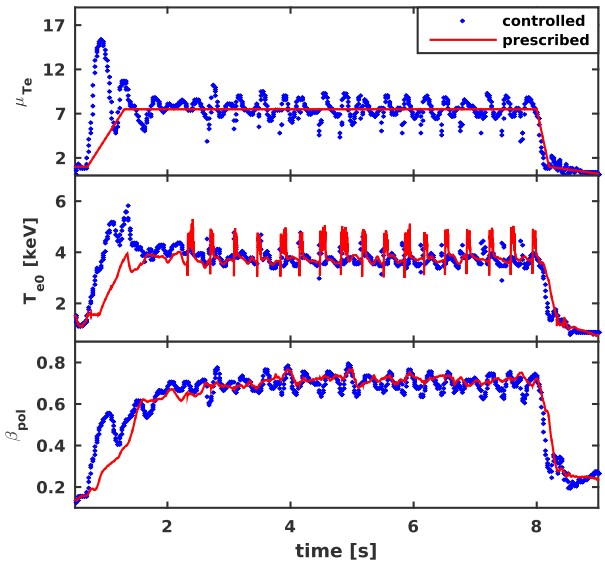

Figure 14. Simulation results for the AUG shot #32546 in case of controlled (blue dots) and prescribed smoothed (red solid) μ_{Te}. Time evolution of the gradient μ_{T_e}, central electron temperature T_{e0} and poloidal beta β_{pol} are presented.

region can be written as

$$\mu_{T_e} = -\frac{dT_e}{d\rho} = -\frac{T_e(\rho_{ped}) - T_e^{BC}}{\rho_{ped} - \rho_{edge}} \tag{19}$$

where $T_e(\rho_{ped})$ is the pedestal electron temperature and T_e^{BC} is the prescribed electron temperature at the plasma edge. If an appropriate scaling law for the pedestal electron temperature (or electron pressure) is defined then μ_{T_e} can be easily found via the definition (19).

A scaling law for the pedestal electron temperature has been defined from the central electron temperature using the constant logarithmic gradient of the "core" region λ_{Te}:

$$T_e(\rho_{ped}) = T_{e0} \cdot e^{(\lambda_{Te}(\rho_{ped} - \rho_{inv}))} \tag{20}$$

while the central temperature has been estimated from the $H_{98,y,2}$ scaling law for the energy confinement time [26] using typical values for the TCV plasma geometry parameters:

$$T_{e0}^{TCV} = 7.5 \cdot 10^3 \cdot (I_p[MA])^{0.93} \cdot (P_{tot}[MW])^{0.3} \cdot (n_{el}[10^{19} m^3])^{-0.6} \tag{21}$$

Inserting this into Eqs. (20, 19) yields the approximation for μ_{Te}^{ff}. For AUG, we have used

$$T_{e0}^{AUG} = 3.3 \cdot 10^3 \cdot (I_p[MA])^{0.93} \cdot (P_{tot}[MW])^{0.3} \cdot (n_{el}[10^{19} m^3])^{-0.6} \tag{22}$$

Figure 14 shows the presence of oscillations for the described controller. However comparison of the electron temperature T_e, poloidal beta and internal inductance

$l_i(3)$ for the cases of controlled and prescribed (i.e. rerunning this simulation using a smoothed μ_{T_e} from the first simulation) μ_{Te} shows that present oscillations in μ_{T_e} do not disturb the physical result too much and even the frequencies of sawteeth oscillations are almost the same. Nevertheless better tuning on the controller gains can improve the simulation result. Note that it is easy and fast to re-run a simulation with $\mu_{Te}^{ff} = \mu_{Te}$(previous simulation) and no feedback control ($K_p = K_i = 0$), this is sometimes performed to check the results.

References

[1] D. Humphreys et al. Novel aspects of plasma control in ITER. *Phys. of Plasma*, 2015. **22** 021806.

[2] D. Moreau et al. Plasma models for real-time control of advanced tokamak scenarios. *Nucl. Fus.*, 2011. **51** 063009.

[3] J. Barton et al. Physics-model-based nonlinear actuator trajectory optimization and safety factor profile feedback control for advanced scenario development in DIII-D. *Nucl. Fusion*, 2015. **55** 093005.

[4] ITER Physics Expert Groups. *ITER Physics Basis, Chapter 3: MHD stability, operational limits and disruptions*, 1999. **39** 2251.

[5] J-Y. Favez et al. Comparing TCV experimental VDE responses with DINA code simulations. *Plasma Phys. Control. Fusion*, 2002. **44** 171.

[6] V. Basiuk et al. Simulations of steady-state scenarios for Tore Supra using the CRONOS code. *Nucl. Fusion*, 2003. **43** 822.

[7] J A. Crotinger et al. *LLNL Report UCRLID-126284*, 1997.

[8] S.H. Kim et al. Full tokamak discharge simulation of ITER by combining DINA-CH and CRONOS. *Plasma Phys. Control. Fusion*, 2009. **51** 105007.

[9] T. Casper et al. Development of the ITER baseline inductive scenario. *Nucl. Fusion*, 2014. **54** 013005.

[10] G. Cenacchi et al. *Rapporto ENEA RT/TIB (88)5*, 1988.

[11] I. Nunes et al. ITER similarity current ramp-down experiments at JET. In *38th EPS Conf. on Plasma Phys. Control. Fusion (Strasbourg, France)*, 2011. **P4.106**.

[12] J.P.S. Bizzaro et al. Modelling the ohmic L-mode ramp-down phase of JET hybrid pulses using JETTO with Bohmgyro-Bohm transport. *Plasma Phys. Control. Fusion*, 2016. **58** 105010.

[13] G. Pereverzev and P. Yushmanov. *ASTRA: Automated System for Transport Analysis (Max-Planck-Institut für Plasmaphysik and Rep. IPP 5 vol 98) (Garching: IPP)*, 2002.

[14] E. Fable et al. Novel free-boundary equilibrium and transport solver with theory-based models and its validation against ASDEX Upgrade current ramp scenarios. *Plasma Phys. Control. Fusion*, 2013. **55** 124028.

[15] S. Fietz et al. Investigation of transport models in ASDEX Upgrade current ramps. *Nucl. Fusion*, 2013. **53** 053004.

[16] F. Felici et al. Real-time physics-model-based simulation of the current density profile in tokamak plasmas. *Nucl. Fusion*, 2011. **51** 083052.

[17] F. Felici. *Real-Time Control of Tokamak Plasmas: from Control of Physics to Physics-Based Control*. PhD thesis, EPFL, Lausanne, Switzerland, 2011. http://infoscience.epfl.ch/record/168656.

[18] F. Felici et al. Control-oriented modeling of tokamak plasmas for real-time plasma monitoring profile control and MHD control. In *43rd EPS Conf. on Plasma Phys. Control. Fusion (Leuven, Belgium)*, 2016. **I4.112**.

[19] E. Maljaars et al. Control of the tokamak safety factor profile with time-varying constraints using MPC. *Nucl. Fusion*, 2015. **55** 023001.

[20] H. Lütjens et al. The CHEASE code for toroidal MHD equilibria. *Comp. Phys. Comm.*, 1996. **97** 219.

[21] F. Hofmann et al. Tokamak equilibrium reconstruction using Faraday rotation measurements. *Nucl. Fusion*, 1988. **28** 1871.

[22] O. Sauter et al. On the non-stiffness of edge transport in L-mode tokamak plasmas. *Phys. of Plasmas*, 2014. **21** 055906.

[23] O. Sauter. *Lausanne Report: Note on the relation between profile scalelengths and lambda's*, 2016. https://infoscience.epfl.ch/record/217967.

[24] D. Kim et al. Simple predictive electron transport models applied to sawtoothing plasmas. *Plasma Phys. Control. Fusion*, 2016. **58** 055002.

[25] F. Felici et al. Non-linear model-based optimization of actuator trajectories for tokamak plasma profile control. *Plasma Phys. Control. Fusion*, 2012. **54** 025002.

[26] ITER Physics Expert Groups. *ITER Physics Basis, Chapter 2: Plasma confinement and transport*, 1999. **39** 2175.

[27] W. Schneider et al. ASDEX upgrade MHD equilibria reconstruction on distributed workstations. *Fusion Eng Design*, 2000. **48** 127.

[28] R. Fischer et al. Bayesian modelling of fusion diagnostics. *Plasma Phys. Control. Fusion*, 2003. **45** 1095.

[29] F. Porcelli et al. Model for the sawtooth period and amplitude. *Plasma Phys. Control. Fusion*, 1996. **38** 2163.

[30] O. Sauter et al. Sawtooth period simulations of TCV discharges. In *Proc. Joint Varenna-Lausanne Int. Workshop on Theory of Fusion Plasmas, Varenna, Italy, August, 1999*, volume ISPP-18, page 403, 1998.

[31] C. Piron et al. Real-time simulation of internal profiles in the presence of sawteeth using the RAPTOR code and applications to ASDEX Upgrade and RFX-mod. *42nd EPS Conf. on Plasma Phys. Control. Fusion, (Lisbon, Portugal)*, 2015. **P1.145**.

[32] O. Kudlacek. *Real Time Plasma State Monitoring*. PhD thesis, UNIPD, Padova, Italy, 2016. http://paduaresearch.cab.unipd.it/9222/.

[33] P.C. De Vries et al. Multi-machine analysis of termination scenarios, providing the specifications for controlled shutdown of ITER discharges. In *26th IAEA Fusion Energy Conference (Naka, Japan)*, 2016. To be published in Nucl. Fusion (2017).

[34] S. Putvinski et al. Halo current, runaway electrons and disruption mitigation in ITER. *Plasma Phys. Control. Fusion*, 1997. **39** B157.

[35] J. Wesson. *Tokamaks*. Oxford Science Publications, New York (USA), 2004.

[36] J. Lister et al. Reducing radial movement in ITER H-L-mode back transitions. In *40th EPS Conf. on Plasma Phys. Control. Fusion (Espoo, Finland)*, 2013. **P1.164**.

[37] M. Leonov et al. Study of ITER plasma current ramp-down scenarios with DINA and ASTRA codes. In *37th EPS Conf. on Plasma Phys. Control. Fusion (Dublin, Ireland)*, 2010. **P2.182**.

[38] F. Imbeaux et al. Current ramps in tokamaks: from present experiments to ITER scenarios. *Nucl. Fusion*, 2011. **51** 083026.

[39] G Becker. Empirical scaling laws for local transport in neutral beam heated plasmas. *Nucl. Fusion*, 1988. **28** 1458.

[40] C. Xu et al. Computing open-loop optimal control of the q-profile in ramp-up tokamak plasmas using the minimal-surface theory. *Plas. Scien. Tech.*, 2013. **15** 403.

[41] M. Sugihara et al. Disruption scenarios, their mitigation and operation window in ITER. *Nucl. Fus.*, 2007. **47** 337.

[42] M. Lehnen et al. Impact and mitigation of disruptions with the ITER-like wall in JET. *Nucl. Fusion*, 2013. **53** 093007.

[43] Y.R. Martin et al. Power requirement for accessing the H-mode in ITER. *Jour. of Phys*, 2008. **123** 012033.